First lithographic results from the extreme ultraviolet Engineering Test Stand

H. N. Chapman[a)]
Lawrence Livermore National Laboratory, 7000 East Avenue, Livermore, California 94550

A. K. Ray-Chaudhuri,[b)] D. A. Tichenor, W. C. Replogle, R. H. Stulen, G. D. Kubiak, P. D. Rockett, L. E. Klebanoff, D. O'Connell, A. H. Leung, and K. L. Jefferson
Sandia National Laboratories, P. O. Box 969, Livermore, California 94551

J. B. Wronosky
Sandia National Laboratories, P. O. Box 5800, Albuquerque, New Mexico 87185

J. S. Taylor, L. C. Hale, K. Blaedel, E. A. Spiller, G. E. Sommargren, J. A. Folta, and D. W. Sweeney
Lawrence Livermore National Laboratory, 7000 East Avenue, Livermore, California 94550

E. M. Gullikson, P. Naulleau, K. A. Goldberg, J. Bokor, and D. T. Attwood
Lawrence Berkeley National Laboratory, One Cyclotron Road, Berkeley, California 94720

U. Mickan and R. Hanzen
ASML, de Run 1110, 5503 LA Veldhoven, The Netherlands

E. Panning, P.-Y. Yan, C. W. Gwyn, and S. H. Lee
Intel Corporation, 2200 Mission College Boulevard, Santa Clara, California 95052

(Received 14 June 2001; accepted 4 September 2001)

The extreme ultraviolet (EUV) Engineering Test Stand (ETS) is a step-and-scan lithography tool that operates at a wavelength of 13.4 nm. It has been developed to demonstrate full-field EUV imaging and acquire system learning for equipment manufacturers to develop commercial tools. The initial integration of the tool is being carried out using a developmental set of projection optics, while a second, higher-quality, projection optics is being assembled and characterized in a parallel effort. We present here the first lithographic results from the ETS, which include both static and scanned resist images of 100 nm dense and isolated features throughout the ring field of the projection optics. Accurate lithographic models have been developed and compared with the experimental results. © *2001 American Vacuum Society.* [DOI: 10.1116/1.1414017]

I. INTRODUCTION

Extreme ultraviolet (EUV) lithography is an attractive next generation lithographic technology since it will support imaging dense 1:1 line–space features smaller than 30 nm and could be introduced as early as the 70 nm mode. The EUV Engineering Test Stand (ETS) is an alpha-class tool that has been developed to demonstrate full-field printing of EUV images and to acquire system learning for equipment manufacturers to develop commercial tools.[1] The ETS has been developed and integrated following an accelerated schedule, using a developmental projection optics box (POB1). A second, higher quality, projection system (POB2) is currently being assembled and characterized,[2] which will replace POB1 in the ETS in early 2002. The ETS has undergone its initial setup, which involved determining the reticle and wafer plane locations, exposure time, illumination conditions, and scan-stage velocity. Static and scanning images have been printed in photoresist and examined by scanning electron microscopy. This article presents the first images that have been obtained. Since the primary purpose of the initial ETS experiments with the developmental set of optics is to assess the quality of the printed images and to determine their dependence on the various subsystems of the ETS, it is important that the lithographic results be compared with models. We give a detailed description of the method to compute aerial images and show initial comparisons with the printed images and with critical dimension (CD) measurements.

II. THE ENGINEERING TEST STAND (ETS)

The ETS is a step-and-scan system that operates at a wavelength of 13.4 nm. The POB is a multilayer-coated, four-mirror, ring-field system with a 0.1 numerical aperture (NA), and a 4:1 image reduction.[3] The field is a 30° sector of the 211 mm radius ring field (96 mm chord length × 6 mm width at the reticle). The reticle is a reflective multilayer-coated ULE substrate that is patterned with absorbing features.[4] A schematic of the ETS, including the vacuum enclosure, support structures, optics, stages, and source assembly, is shown in Fig. 1.

A. EUV source

The EUV radiation is generated from a laser-produced plasma by focusing a pulsed Nd:YAG beam onto a xenon

a)Electronic mail: chapman9@llnl.gov
b)Present address: KLA-Tencor, 160 Rio Robles, San Jose, CA 95134.

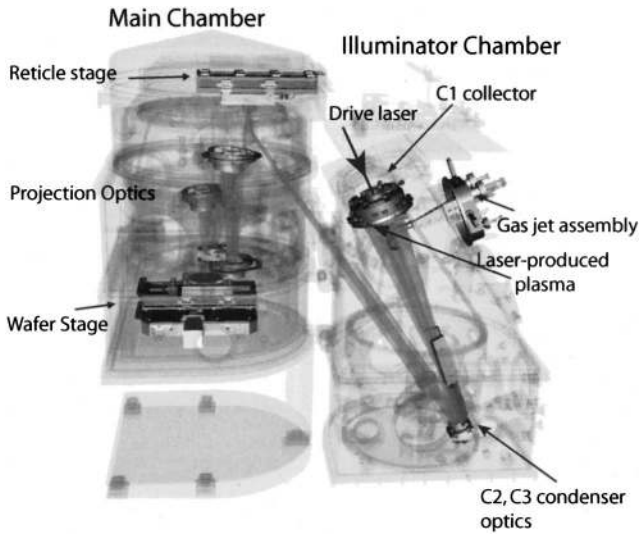

FIG. 1. Solid-model schematic of the EUV ETS.

cluster target.[5] The source diameter is approximately 300 μm. The initial lithography results presented here were performed with a 40 W laser, which delivers 0.11 mW/cm^2 EUV power at the wafer. Tests of a higher-power laser, developed by the TRW Corp., have been performed in a separate source development facility adjacent to the ETS. Measurements show that 10–20 mW/cm^2 can be expected at the wafer plane in the ETS, depending on source conditions, following integration of this high-power source. This compares with the desired EUV power density of 22.6 mW/cm^2 at the wafer that would support ten 300 mm wafer/s operations.

B. Illuminator

The condenser system collects the EUV light from the source and provides quasistationary illumination across the ring field, with a six-channel pupil fill.[6] The collection solid angle is 1.68 sr. The collector and subsequent condenser optics are divided into six channels. Each channel provides Köhler-critical illumination that produces an arc-shaped beam footprint on the mask to match the ring field of the projection optics at the reticle plane, and an angular illumination of approximately $\sigma_V = 0.3$ and $\sigma_H = 0.015$. The intensities of all six channels overlap at the reticle plane, but the angular distribution of each is displaced to give an effective pupil fill of $\sigma = 0.7$. The measured reticle plane illumination intensity and uniformity are shown in Fig. 2. The modeled pupil fill, for the central field point, is shown in Fig. 3(a). Note that as the field point moves azimuthally around the arc each channel in the condenser exit pupil rotates by the corresponding angle. Thus, the open-frame pupil fill, which is the fill integrated over all field points, shows channels that are bow-tie shaped. Figure 3(b) shows the open-frame pupil fill, observed experimentally on a scintillator located at the projection optics pupil.

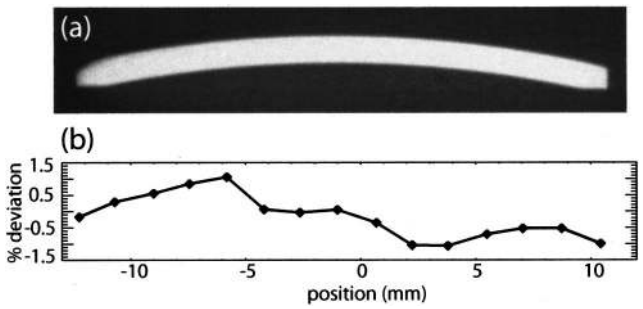

FIG. 2. (a) Open frame resist exposure at the wafer and (b) deviation of the scan-averaged intensity from the mean. The width of the illumination is 24 mm at the wafer.

C. Projection optics

The developmental projection optics box (POB1) was assembled[1] and characterized by both visible-light and EUV interferometry.[7] With both techniques, the system wave front error was measured at 45 field points throughout the ring field. A contour plot of the rms wave front error across the ring field, as measured by visible-light interferometry, is shown in Fig. 4(a). The mean rms wave front error across the field is 1.20 nm ($\lambda/11$), in a 36-term Zernike polynomial decomposition, and varies between 0.90 and 1.4 nm. On average, the difference between the EUV and visible-light measurements was 0.25 nm rms. This is an indication of the accuracy of the wave front measurement. The visible-light interferometer measures wave front aberrations in the projection optics pupil up to a spatial frequency of 54 cycles/pupil radius (i.e., per NA). The measured aberration map at the central field point is shown in Fig. 4(c). The rms wave front error for this map is 2.02 nm. At this field point, the rms wave front error in a 36-term Zernike decomposition is 0.94 nm, so the residual power (up to a frequency of 54/NA) is 1.79 nm. This structure, which is quite noticeable in Fig. 4(c), is not an artifact of the measurement but is due to the polishing process of manufacturing the mirrors. The wave front error in these frequencies will lead to short-range flare, which will cause a loss of image contrast, as discussed in Sec. III. Initial measurements of POB2 show a residual rms error of $\sim$1.0 nm.

Aberrations at spatial frequencies greater than 54/NA have been inferred statistically, using EUV scattering measurements of the individual mirrors of the POB. The scatter-

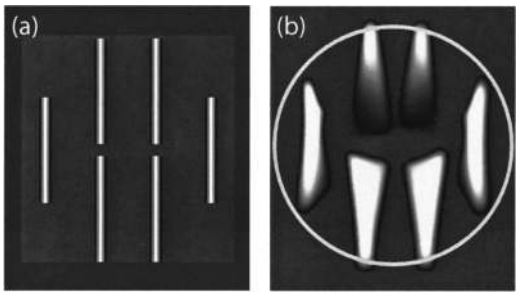

FIG. 3. (a) Modeled pupil fill for the central field point. (b) Open frame pupil illumination, measured on a scintillator at the pupil of the POB. The circle denotes $\sigma = 0.7$.

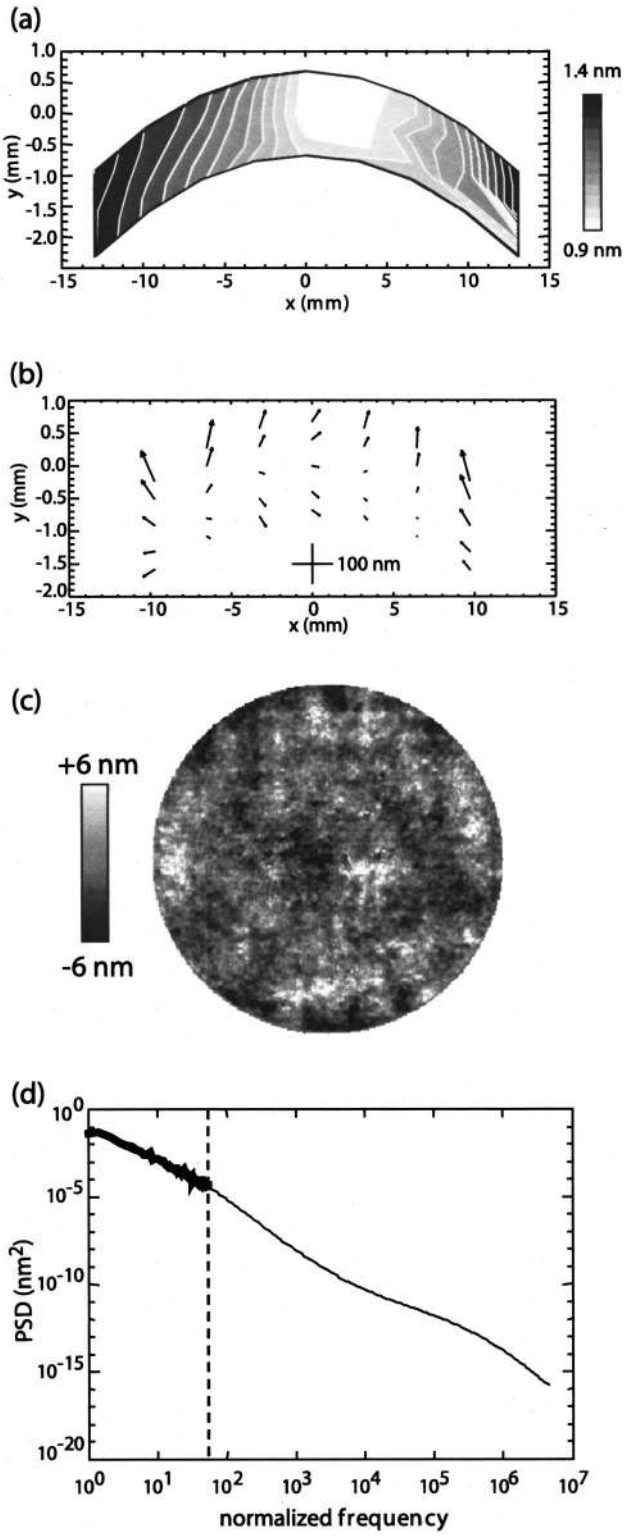

FIG. 4. POB1 is extensively characterized: (a) rms wave front error as a function of field location at the wafer plane, as measured by visible-light interferometry. (b) Vector plot of distortion at the wafer plane, determined by Leica IPRO measurements of printed fiducials. The mean distortion is 32 nm, and the maximum is 80 nm. (c) Aberration map at the central field point. (d) Power spectral density of the system aberration as a function of normalized frequency (number of cycles per pupil radius), determined from scattering measurements of the mirrors (thin line) and from the aberration map in (c) (thick line). The integrated power in frequencies 0–54/NA is 2.02 nm, and the total integrated power is 2.33 nm.

ing measurements are compiled[8] into a system wave front PSD, as shown in Fig. 4(d). These higher frequencies lead to long-range flare, which also reduces image contrast.

The distortion (or image-placement error), shown in Fig. 4(b), was measured from static prints made in the ETS. Printed images of fiducial patterns were examined using a Leica LMS IPRO wafer inspection instrument. IPRO measurements were made on many exposures printed at various locations across a wafer to average random error in the IPRO and error due to wafer nonflatness. The measurement error was estimated to be 4 nm. The distortion could be further improved (to a mean of 27 nm, with a maximum error of 50 nm) by adjusting the tilts of the reticle and wafer planes. The static distortion field impacts the quality of scanned images, as is described in Sec. IV C. In a scan, the distortion causes image motion during the exposure, which results in a blurring of the printed image.

D. Scanning stages

Scanned images are formed by scanning the reticle at a constant velocity through the illuminated field of the projection optics. The wafer is synchronously scanned at a quarter of the mask velocity so that the scanned image appears stationary on the wafer. Any deviation from true synchronization, either in speed or direction, will cause a blur of the printed image. A feedback control system provides the synchronization of the stages and dynamically references these to the POB structure.[9] In terms of stage operation, static imaging is simply scanning at zero velocity. The stages are still actively controlled in this case and dynamically tracked to the POB structure. Several full-field scanned images, each measuring 24 mm×32.5 mm, have been printed. The reticle scan speed was approximately 40 μm/s (limited by the EUV intensity). At zero velocity and 40 μm/s the jitter of the reticle stage is below 5 nm rms and the jitter of the wafer stage is below 10 nm. The stages have also been tested at speeds of 20 mm/s, and were seen to meet the same jitter performance.

III. IMAGE MODELING

A primary goal of the initial lithographic tests of the ETS, using the developmental set of projection optics, is to understand the quality of the printed images and how the various subsystems impact those images. By comparing images and measurements of image metrics (such as linewidth) to models we can identify and resolve problems that arise in integrating the components of the ETS.

It was found that a conventional model based on one-dimensional periodic objects could not accurately model ETS images. The sparse pupil fill, coupled with the high-spatial-frequency nature of the wave front map (see Figs. 3 and 4), leads to significant differences in the printing of one-dimensional (1D) periodic objects versus 2D elbow patterns.

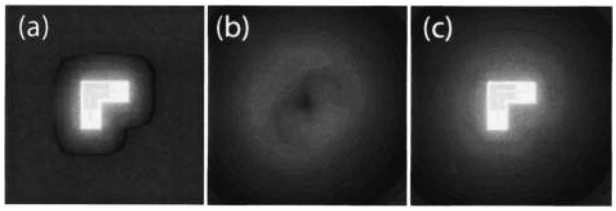

FIG. 5. Computed images of 100 nm elbow patterns: (a) high-resolution partially coherent image, (b) low-resolution incoherent image, based on the PSD, and (c) sum of (a) and (b). The contrast of the images has been reduced (gamma of 3%) to show the short-range flare.

In the 1D periodic object case, the discrete diffraction orders only sample small regions of the projection optics aberration map, even when considering all illumination directions from the condenser. A small change in linewidth completely changes the sampled regions of the aberration and may lead to a completely different effect on the image. The 2D elbow pattern produces a continuous diffraction pattern and so this computation does not exhibit these effects. As an example, the predicted horizontal–vertical focal shift caused by astigmatism varies strongly and erratically with linewidth in the 1D calculation. A 0.5 nm addition of astigmatism to the wave front gave a focal shifts of 0.9, 0.5, and 0 μm for linewidths of 80, 100, and 200 nm, respectively. This behavior is contrary to that observed in the ETS, and clearly the 1D calculations are not useful for estimating the degree of astigmatism in printed images (see Sec. IV A).

The 2D images are computed as the sum of a *deterministic* and a *statistical* component. The deterministic component is a partially coherent image that is computed from a given object pattern, a measured wave front error map (depending on the field point being considered), and an illumination pupil fill. The wave front map includes spatial frequencies up to 54/NA, which corresponds to a maximum extent of the point-spread function (PSF) of 7.2 μm, for the 0.1 NA and 13.4 nm wavelength. An example of such a computed aerial image is given in Fig. 5(a). When modeling images of larger extent, or objects that are in an extended bright field, we must include aberrations of higher spatial frequency. These are characterized by the power spectral density (PSD), shown in Fig. 4(d). It is assumed that at these higher frequencies the wave front error is homogeneous and isotropic across the pupil and across the field. This implies that the image caused by scattering from these frequencies does not depend on pupil fill.[8] Hence, this image component may be computed as a convolution of the object pattern with the long-range intensity PSF (which is directly proportional to the PSD).

The two components of the image computation can also be categorized as high and low resolution. In general, a large area of the mask may contribute intensity to the image region of interest due to the high-frequency aberration component of the optics. In this case, the low-resolution component is computed over that large area, with a large pixel sampling to reduce computation time. The appropriate subregion of that image is then extracted and extrapolated to the high-resolution image, as shown in Fig. 5(b). The low-resolution computation may be further split into various resolution regimes, so it is possible to include intensity contributions from the entire illuminated field. In this way the effects of flare (that is, high-frequency aberrations) can be accurately modeled for any mask pattern. The final (high-resolution) computed image is the sum of the components, as shown in Fig. 5(c).

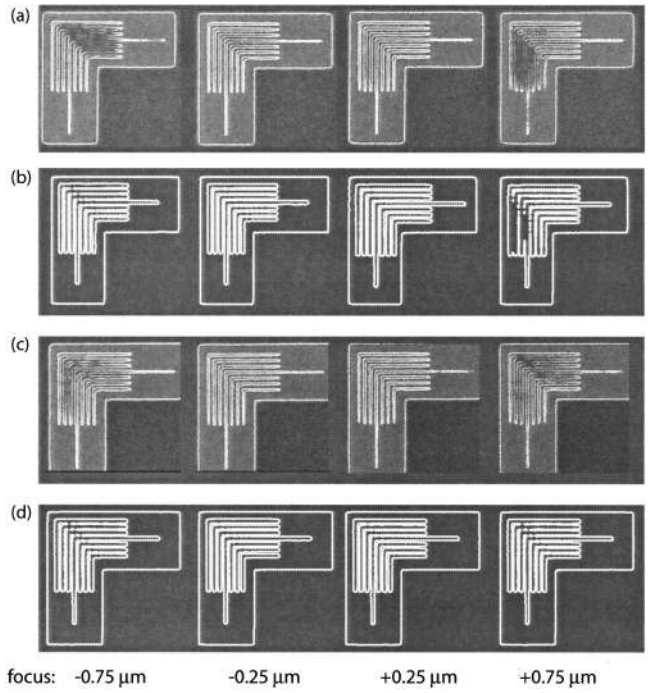

FIG. 6. Through-focus resist images of 100 nm dense elbow patterns (a) prior to aberration correction compred with modeled images with −0.5 nm added astigmatism (b). (c) Resist images after correction of the projection optics by 1.0 nm of astigmatism compared with modeled images with +0.5 nm added astigmatism (d).

IV. INITIAL TOOL SETUP

A. *In situ* aberration correction

Our initial imaging tests on the ETS were performed 9 months after interferometric characterization of POB1. Nevertheless, the initial static imaging results indicated a remarkable mechanical stability of the POB, with the only change being a small drift in astigmatism. This can be seen in Fig. 6(a), which displays some of the first static resist images from the ETS. The degree of astigmatism was found by correlating printed images of elbow patterns at various linewidths, foci, and dose, with partially coherent modeled images. The best correlation was found when −0.5 nm rms of 0°–90° astigmatism was added to the model. Modeled resist images, based on a simple intensity threshold, are shown in Fig. 6(b). For our off-axis ring-field POB, astigmatism is the most sensitive aberration that is induced by any motion of any of the mirrors. Such a small value of astigmatism implies that none of the mirrors could have drifted by more than 7.5 μrad over the 9 month period since the POB was aligned and

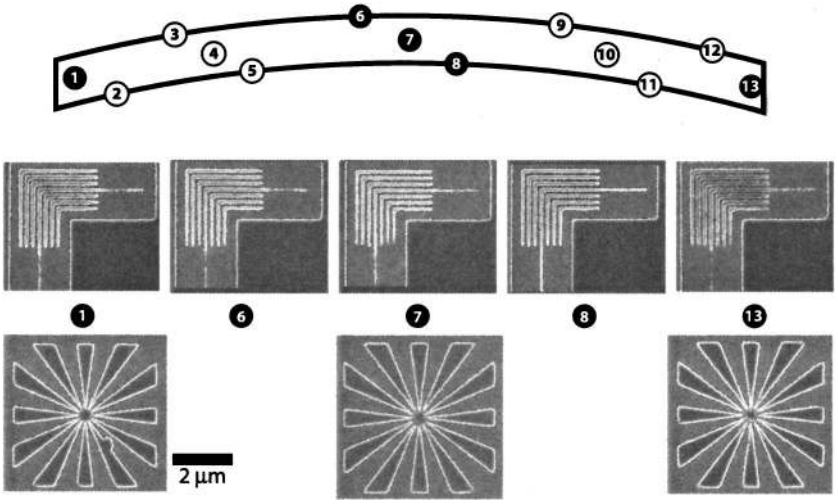

FIG. 7. Selection of static resist images of 100 nm elbow patterns and star patterns from various locations throughout the ring field, as denoted by the circled numbers and the map of the ring field. The scale bar refers only to the star patterns.

characterized. Furthermore, analysis shows that other aberrations such as coma and spherical aberration could not have changed by more than 0.02 nm. To first order, a tilt of any of the four mirrors can be used to correct the observed astigmatism. The mirror $M4$ was chosen since this has the lowest impact on image placement error.

Modeling, in fact, showed that the optimum value of astigmatism for the 100 nm features is $+0.5$ nm rms. Therefore a correction of 1 nm rms astigmatism (uniform across the field) was induced by tilting $M4$ by 6.0 μrad. The resulting images after adjustment and model predictions are shown in Figs. 6(c) and 6(d), respectively.

B. Full-field static images

Static images were examined throughout the field, and compared with computed images, to ensure that the illumination was best aligned to the well-corrected field of the projection optics. The wafer was tilted to correct for the focus variation across the ring field. However, further wafer and mask adjustments must still be carried out to further reduce the static distortion field (this is a consequence of nontelecentricity at the reticle plane). A sample of resist images of elbow and star patterns from various locations throughout the field is shown in Fig. 7. The trends observed in the prints agree with the modeled images. For example, the known increased wave front aberration at the right edge of the field leads to the degraded image performance there.

C. Scanned images

To print scanned images, the velocity (i.e., speed and direction) of the wafer relative to that of the reticle must be optimized. The residual velocity error of the wafer, which is the vector difference between the velocity of the scanned image and the wafer stage, can be characterized by its orthogonal components: stage magnification error and stage skew error. A stage magnification error results in a blur function that extends in the scan direction, whereas a skew error leads to image motion (relative to the scanned wafer) in the cross-scan direction. The skew error depends on image rotation caused by the projection optics and error in the parallelism of the stages, and was determined from a series of exposures where the stage skew is varied. The stage magnification error was predicted from the IPRO static distortion measurements [see Fig. 4(b)] to be ± 82 ppm. The optimum stage skew and stage magnification corrections were found, from a series of prints where both parameters were varied, to be -680 μrad and $+75$ ppm, respectively. After subtracting the magnification error from the static distortion field, the predicted amount of the blur due to the projection optics distortion for the central field point is approximately 10 nm.

Scanned printed images from the ETS are shown in Fig. 8. All of these images are from the center of the field and the scan direction is vertical on the page. Analysis of the linewidth and contrast of the scanned images has not yet been completed. However, the scanned 100 nm elbow printed pat-

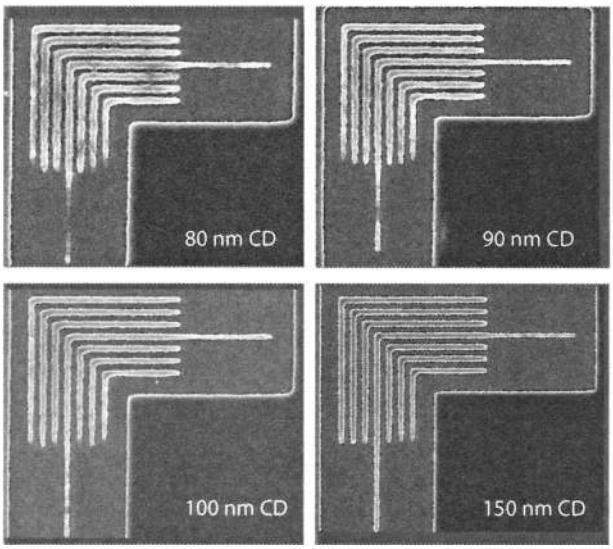

FIG. 8. Scanned resist images of elbow patterns, from the center of the field. The scans were acquired with the full 1.5 mm width of the ring field illuminated. The dose was optimized separately for each linewidth. Each image has been separately scaled in size.

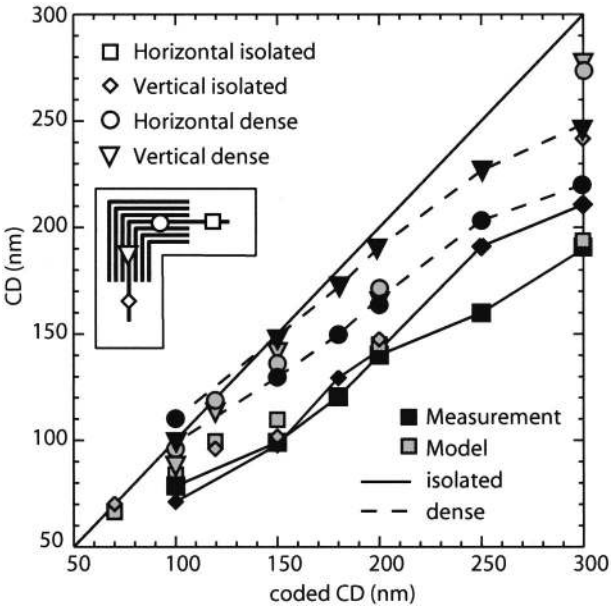

FIG. 9. Measured and modeled linewidths of the horizontal and vertical, dense, and isolated features of elbow patterns printed at a constant dose.

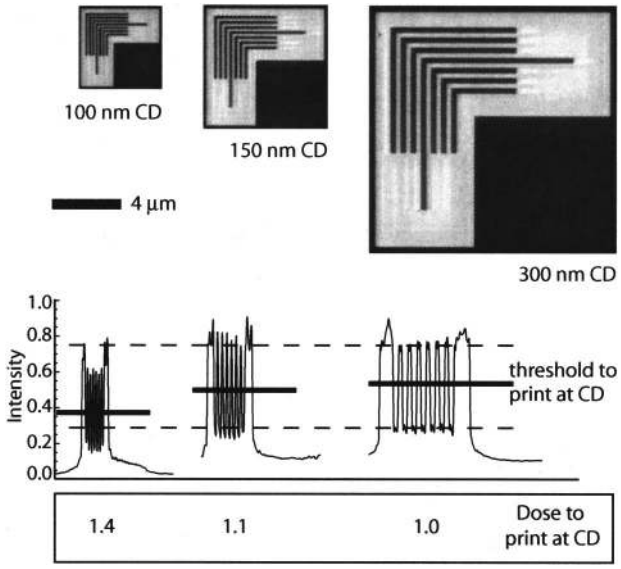

FIG. 10. Modeled aerial images of elbow patterns of vairous sizes showing that, for these particular mask patterns, flare increases with increasing feature size.

terns are almost indistinguishable from the static images. This shows that scanning has minimal impact on the image quality, as is predicted given the 10 nm blur (Gaussian half width) caused by static distortion.

V. STATIC LITHOGRAPHIC PERFORMANCE

Measurement of the width of lines in images of 1:1 line:space elbow patterns, printed at constant dose in 100 nm thick Shipley 2D positive-tone resist, results in the CD linearity plot shown in Fig. 9. It is seen that there is an isodense bias of about 40 nm, and that the printed CD increases as 80% of the coded CD of the pattern. The aberrations and short-range flare of the projection optics can explain both of these effects, and the results are in good agreement with modeled images. It is well understood that a 1 nm ($\lambda/13$) 36-term Zernike aberration leads to greater contrast loss in isolated lines than dense lines. The flare in the projection optics exacerbates this contrast loss. The flare (in combination with the particular mask pattern used in these measurements) also causes the reduction of linewidth with increasing CD. The elbow patterns are dark lines in a bright L-shaped island in an almost entirely dark field. Thus, only points in the bright L-shaped island contribute scattered light into the line patterns. The area of this bright region increases as the square of the CD. That is, larger patterns have a higher contribution of flare, and so larger CD patterns require less dose to print. For example, as shown in Fig. 10, at the required dose for 100 nm features, the 300 nm features will be overexposed and the cleared lines in resist will be smaller than ideal.

An additional observation from the printed images is that horizontal dense lines print approximately 20 nm wider than vertical dense lines. This may be due to vibration in the projection optics. This will be investigated further as soon as additional diagnostics, including an aerial-image monitor, are implemented this year.

IV. CONCLUSIONS

The EUV ETS is operational in scanning and static imaging modes. The tool integration and initial testing were accomplished very quickly. The first EUV images were printed 6 months ahead of our original schedule, and scanned images followed only 3 weeks later. Part of the initial setup involved an *in situ* correction of astigmatism. It was found that the 0.5 nm rms observed astigmatism could easily and accurately be corrected with a controlled tilt of one the POB mirrors. Static resist images of dense 1:1 elbow patterns, ranging in size from 100 to 300 nm, show as-expected image quality across the entire ring field of the projection optics. The 100 nm patterns, including both dense and isolated features, are well resolved throughout the entire field, and 80 nm patterns are well resolved at the center of the field, where aberrations are lowest. Currently, the only deviation from the expected ETS performance is a 20 nm $H-V$ bias in the static printed patterns. Full-field (24×32.5 mm^2) scanned images have been acquired. The scanned images of dense 100 nm elbow patterns are almost indistinguishable from the static images, proving that neither stage motions nor the POB static distortion field impacts the image quality.

Lithographic characterization of the ETS has only just begun, and the near-term plans include the measurement of image contrast and line-edge roughness of static images, CD characterization of scanned images, and measurement of flare throughout the field. We will continue to compare measurements with simulations to provide a firm foundation for system learning. These will be followed by the full-power source upgrade and then the installation of the higher quality projection optics.

ACKNOWLEDGMENTS

This work was performed by the University of California Lawrence Livermore National Laboratory under the auspices of the U.S. Departemnt of Energy, Contract No. W-7405-ENG-48, by Sandia Naitonal Laboratories under the auspicies of the U. S. Department of Energy, Contract No. DE-AC04-94AL85000, and by the Lawrence Berkeley National Laboratory under the auspices of the U. S. Department of Energy Office of Basic Energy Sciences. Funding was provided by the Extreme Ultraviolet Limited Liability Corporation under a Cooperative Research and Development Agreement.

[1]D. A. Tichenor *et al.*, Proc. SPIE (in press).
[2]P. Naulleau, K. A. Goldberg, P. Batson, S. Rekawa, P. Denham, and J. Bokor, J. Vac. Sci. Technol. B, these proceedings.
[3]D. W. Sweeny, R. Hudyma, H. N. Chapman, and D. Shafer, Proc. SPIE **3331**, 2 (1998).
[4]S. Hector and P. Mangat, J. Vac. Sci. Technol. B, these proceedings.
[5]G. D. Kubiak, L. J. Bernardez, K. Krenz, and W. C. Sweatt, Proc. SPIE **3676**, 669 (1999).
[6]W. C. Sweatt, in *OSA Proceedings on Soft X-Ray Projection Lithography*, edited by A. M. Hawryluk and R. H. Stulen, 1994, Vol. 18, pp. 70–72.
[7]K. A. Goldberg, P. Naulleau, P. Batson, P. Denham, E. Anderson, H. Chapman, and J. Bokor, J. Vac. Sci. Technol. B **18**, 2911 (2000).
[8]D. G. Stearns, D. P. Gaines, D. W. Sweeney, and E. M. Gullikson, J. Appl. Phys. **84**, 1002 (1998).
[9]J. B. Wronosky *et al.*, Proc. SPIE **3997**, 829 (2000).